Forcing processes of the summertime circumglobal teleconnection pattern in a dry AGCM

Soichiro Yasui[1†] **and Masahiro Watanabe**[2*]

1: Graduate School of Environmental Science, Hokkaido University

2: Center for Climate System Research, University of Tokyo

Journal of Climate

Submitted on May 27, 2009

Revised on September 30, 2009

Revised on November 6, 2009

* Corresponding author:

Dr. Masahiro Watanabe

Center for Climate System Research, University of Tokyo

5-1-5 Kashiwanoha, Kashiwa, Chiba 277-8568, Japan

E-mail: hiro@ccsr.u-tokyo.ac.jp

† Present affiliation :

Japan Meteorological Agency, Japan

ABSTRACT

To better understand the predictability of the wave-like circumglobal teleconnection (CGT) pattern prevailing during boreal summer, two sets of experiments are performed using a nonlinear dry atmospheric model. Each experiment consists of a ten-member ensemble of 26 yr integrations driven by the diabatic heating derived from reanalysis data; one with the monthly climatological mean heating (CLIM), and another with the monthly heating for 1979-2004 (HIST). Both well reproduce the observed summer mean state, as well as the low-frequency variance distribution.

The CGT pattern identified in the monthly meridional wind anomalies at 200 hPa shows zonally oriented wave packets over Eurasia. The simulated CGT has a nearly identical phase structure with observations, and with little difference between the CLIM and HIST. While this indicates that the origin of CGT lies in the internal dry dynamics, the ensemble mean of the CGT in HIST is partly controlled by the slow variation in the heating field, as indicated by the high potential predictability of the simulated CGT pattern. Diagnoses using the linearized model demonstrate that the heating anomaly most responsible for the CGT-like steady response is located over the East Mediterranean region, where the heating may be coupled with the CGT pattern. In addition to the heating near the CGT, remote heating and cooling anomalies over North America and equatorial Africa are found effective at exciting stationary Rossby waves trapped on the Atlantic and Asian jets. It was thus suggested that the mechanisms generating the heating anomalies over these regions are the key for the predictability of the CGT pattern.

1. Introduction

Large-scale atmospheric circulation in the extratropics fluctuates in its own dynamics, which involve nonlinear interaction among eddies that have various horizontal scales and a wide range of time scales. The fluctuations inherent to the extratropical atmosphere are generally unpredictable beyond a threshold of about two weeks due to their chaotic nature. On the other hand, changes in slowly varying components of the climate, such as sea surface temperature (SST), also give rise to the large-scale circulation variability, which may be more predictable when the boundary conditions are given. The extent to which the observed circulation variability is forced by the underlying SST anomalies has been examined in many studies by an ensemble of atmospheric general circulation model (AGCM) simulations, driven by the history of observed SST (e.g., Gates et al. 1999). This type of AGCM experiments, often called an AMIP run, provides clues to the forcing mechanisms of the atmospheric teleconnection patterns.

When SST anomalies cause circulation changes, the variable that explicitly forces the atmosphere is the diabatic heating anomaly primarily associated with the convective precipitation, which is affected by SST anomalies. In the AGCM, diabatic heating is an internal process, and is represented by parameterization schemes for cumulus clouds, shallow clouds, radiation, and turbulence. Therefore, the anomalous diabatic heating in AGCMs tends to contain large errors even if the SST is correct; this is a major caveat of the AMIP-type experiment. One idea to avoid such errors is the use of a dry AGCM, or the dynamical core, which can produce a robust circulation response to a given external forcing (Held and Suarez 1994). Instead of using parameterization schemes, the dry AGCM is run with given diabatic heating fields. Several studies have

shown that such a simple AGCM can reproduce the mean circulation (Hoskins and Rodwell 1995; Hall 2000) and variability (Peterson et al. 2002; Sardeshmukh and Sura 2007; Lin et al. 2007). This is the type of atmospheric model that we construct and use for exploring the forcing processes of the Northern Hemisphere (NH) summer circulation variability in this study.

In boreal summer, baroclinic disturbances are not as active as in the winter season, and large-scale teleconnection patterns are also less prevalent. Yet, a distinct teleconnection pattern that has a zonally oriented wave-like structure is known to dominate in NH summer (e.g., Terao 1998; Lu et al. 2002; Enomoto 2004; Lau et al. 2004; Ding and Wang 2005, hereafter DW). This wave-like teleconnection is typically identified in the monthly mean meridional wind fields, and has the characteristics of stationary Rossby waves trapped on a subtropical jet (Hoskins and Ambrizzi 1993). Since the anomaly pattern is more like circumglobal, we hereafter call it the circumglobal teleconnection (CGT), following Branstator (2002), although there are alternative names, such as the “silk road pattern” (Enomoto et al. 2003) and the “Tokyo-Chicago express” (Lau et al. 2004). The CGT pattern was first detected during NH winter (Hsu and Lin 1992), and appears ubiquitous to the extratropical circulation, where the jet waveguide exists (Ambrizzi et al. 1995).

The winter CGT pattern over Eurasia frequently appears in association with the North Atlantic Oscillation (NAO), as reported by Branstator (2002). The connection between the NAO and CGT is reasonable because the decay of the NAO can give rise to a wave source that excites the CGT downstream (Watanabe 2004). In summer, the relationship between the CGT and the Asian summer monsoon has been extensively discussed. For example, Krishnan and Sugi (2001) found a wave-like circulation

anomaly on the Asian jet concurrent with the interannual variability in the Baiu rainfall, and argued for the possibility that the CGT connects the Baiu and the Indian monsoon variability. DW examined the CGT in reanalysis data, and proposed a chain of interaction between the CGT and the Indian monsoon rainfall variability: one interaction involves the wave train originating over the North Atlantic and modulating the monsoon rainfall activity, and another interaction involves anomalous monsoon heating influencing the downstream development of the CGT (their Fig. 15). This two-way interaction between the CGT and the monsoon heating is attractive, but has not been verified because DW speculatively obtained this scenario from observed statistics. In short, the issues of what forces the summertime CGT pattern and how much of the observed CGT is predictable are still open questions.

One can analyze the CGT simulated in AMIP experiments or atmosphere-ocean coupled GCMs to gain insight into its forcing mechanisms. As mentioned above, however, the heating error problem remains. Moreover, state-of-the-art climate models cannot necessarily realistically reproduce the CGT because of the bias in the mean waveguide structure (Kosaka et al. 2009). In the present study, we therefore use a dry AGCM forced either by the climatological or historical heating fields that are the products of reanalysis, and attempt to clarify the above questions. As shown later, despite the fact that the model is simpler than the full AGCM, the dry AGCM well reproduces the summer mean state and the CGT. Since the diabatic heating is completely controlled in the dry AGCM experiments, we can identify an optimal spatial structure of the heating anomaly that explains the largest fraction of the forced CGT signal.

This paper is organized as follows. In the next section, the numerical models and observational data are described. In section 3, the mean states, including the variance fields, are presented, and the high potential predictability of the monthly mean anomalies in a dry AGCM is demonstrated. The simulated CGT pattern is then compared with observations in section 4, in which the forcing mechanism is thoroughly examined with the help of linear model diagnoses. Section 5 gives a summary and discussion.

2. Models and data

a. Observational data

The observations used in this study are derived from the Japanese reanalysis project (JRA-25, Onogi et al. 2007). The JRA-25 is jointly carried out by the Japan Meteorological Agency (JMA) and the Central Research Institute of Electric Power Industry (CRIEPI), and provides atmospheric data for 1979–2004 by using the 3DVAR technique applied to the JMA operational model, which has a resolution of T106 L40. The data have the horizontal resolution of 2.5° × 2.5° and are provided either on 23 pressure levels or on 40 eta levels, the latter following the model's vertical coordinates. We use the monthly mean fields, which are then converted to anomalies by subtracting the climatological mean for 1979–2004. In the present study, variables derived from the data assimilation model are analyzed in addition to standard meteorological fields. Specifically, the diabatic heating terms are used to drive the model that is described in the subsequent section. In addition to the JRA-25 data, monthly SST data on a 1° × 1° grid derived from the Hadley Centre (Rayner et al. 2003) are used in section 4c.

b. Nonlinear baroclinic model

We use a simplified AGCM, or nonlinear baroclinic model (hereafter referred to as the NLBM), based on primitive equations on a sphere. The horizontal resolution is T42 and 20 vertical layers are adopted on σ surfaces. The NLBM is derived from the CCSR/NIES/FRCGC AGCM (Watanabe 2009), in which a simplification is made to the physical processes incorporated into the AGCM by eliminating water vapor from the prognostic equations. Instead, the diabatic heating associated with the condensation/ evaporation and radiative processes is prescribed by externally given data. Such terms as were needed to maintain a realistic mean state in the NLBM are also added to either the momentum or thermodynamic equations as follows:

$$\rho\frac{\partial \mathbf{v}}{\partial t}+\cdots=-\rho\alpha_R\mathbf{v}+\frac{\partial \mathbf{F}_v}{\partial\sigma} \quad , \tag{1}$$

$$\rho c_p\frac{\partial T}{\partial t}+\cdots=\rho c_p\beta(T^*-T)+Q+\frac{T}{\theta}\frac{\partial F_\theta}{\partial\sigma} \quad , \tag{2}$$

where the first term on the right-hand-side of (1) represents the Rayleigh friction applied to the stratosphere, and the coefficient α_R is level-dependent (8, 8, 8, 8, 12, 12, 12, 16, 16 d)$^{-1}$ from the model top, i.e., $0.008 \le \sigma \le 0.23$. The temperature field is forced by the aforementioned diabatic heating, *Q*, and very weak Newtonian cooling as expressed by the restoration to the reference temperature, T^*, with the timescale of $\beta = (25\ \mathrm{d})^{-1}$. The Newtonian cooling is added to maintain the radiative balance, which is not accomplished by a given radiative forcing, and is not crucial to the model's behavior. The reference temperature is simply defined by the zonal-mean climatology derived from the JRA-25 reanalysis.

The last terms on the right-hand-side of (1)-(2) are the vertical transport of the momentum and heat due to turbulence, and parameterized as

$$\mathbf{F}_v = \begin{cases} -\rho C_M |\mathbf{v}| \mathbf{v} & \text{at } \sigma = 1 \\ K_M \dfrac{\partial \mathbf{v}}{\partial \sigma} & \text{else} \end{cases}, \tag{3}$$

$$F_\theta = \begin{cases} -\dfrac{1}{\tau}(\theta^* - \theta) & \text{at } \sigma = 1 \\ K_H \dfrac{\partial \theta}{\partial \sigma} & \text{else} \end{cases}, \tag{4}$$

where K_M and K_H are the mixing coefficients, calculated following the level-2 turbulent closure (Mellor and Yamada 1982). Since the NLBM lacks the land model, the surface sensible heat flux is replaced by a simple relaxation to the monthly climatological potential temperature, θ^*, derived from JRA-25 with a timescale of 3 h. The bulk transfer coefficient for momentum, C_M, is calculated by a parameterization by Louis (1979), except that the surface roughness is doubled over land.

In most previous studies using the dry AGCM, the diabatic heating was estimated as a residual of the thermodynamic equation (e.g., Hoskins and Rodwell 1995). The major reason for using the "residual heating" is that the heating fields derived from an objective analysis have contained errors arising from the dependence on the parameterization incorporated in the operational model. The residual heating, however, may also not be correct, since it includes all of the errors in the state variables. Fortunately, recent reanalyses provide improved accuracy for the 3D heat and energy budgets (Trenberth and Smith 2008). Therefore, we use the JRA-derived diabatic heating fields for forcing in the NLBM, even recognizing that they are dependent on the parameterization, in particular for cumulus convections. In the quality control procedure, we found some artificial long-term variability due to inappropriate bias correction to the satellite data. Therefore, the low-frequency components defined by applying a 10 y low-pass filter were removed from the heating fields in advance.

The diabatic heating consists of the sum of the condensation heating due to convective and non-convective clouds (the latter referred to as the large-scale condensation) and the shortwave and longwave radiations. The data are originally monthly means, and are linearly interpolated in the time domain to drive the NLBM. It should be noted that the heating associated with the surface sensible flux is not included because it is internally calculated in (2). An example of the imposed heating is presented in Fig. 1, which shows the vertically averaged climatology in summer (June, July, and August, denoted as JJA). The primary heat source is found to be over the convective regions of the equatorial Pacific and Atlantic Oceans, the western tropical Pacific, and the Asian monsoon area, whereas radiative cooling dominates over the subtropics, in particular the oceanic regions. Since the JRA-25 reanalysis was carried out with the horizontal resolution of T106, it resolves a fine horizontal structure associated with orography and the small-scale circulation; the former is found over the continents and is likely to be robust, but the latter may partly come from the cumulus parameterization employed by the reanalysis model. It is not quite sure whether the small-scale features in heating are reliable, but most of them are much smoothed when interpolated onto the T42 grids.

We performed two sets of numerical experiments, each of which consisted of a ten-member ensemble for a 26 y-long integration from Jan 1979 to Dec 2004. One is a climatological run, denoted as the CLIM, in which the monthly climatological heating is given to the NLBM, and the other is a historical run (HIST), where the monthly historical heating is used. The initial conditions are randomly taken from another 30 y integration with the climatological heating. A comparison of these two experiments, in addition to a comparison with the reanalysis, enables us to discuss the role of the

heating variability in forcing the circulation anomalies. In the following section, data during 1979, which is regarded as the spin-up period, are excluded from the analysis.

c. Linear baroclinic model

In order to elaborate the forcing processes in the NLBM, its linear version is also used. This model, called the linear baroclinic model (LBM), is an exactly linearized set of primitive equations, and has been extensively used for diagnostic studies of atmospheric teleconnections (Watanabe and Kimoto 2000, 2001; Watanabe and Jin 2004, Pan et al. 2006). With the same resolution as the NLBM, the LBM is used to solve the steady problem with the summer basic state and heating anomaly taken from the NLBM. Since the linear operator must be stable for the steady problem, we adopt a biharmonic horizontal diffusion with a timescale of 2 h for the smallest-scale wave; this is stronger than that adopted in the NLBM. The turbulent mixing is approximated by a linearized Mellor-Yamada closure, which is described in the appendix.

3. Mean state and variability in the NLBM

a. Climatology and variance

As a prelude to the analysis of the simulated CGT variability, the extent to which the NLBM can reproduce the summer mean state and mean variance distribution is examined. In Fig. 2, we compare the JJA-mean climatology in the CLIM with that in the JRA-25 reanalysis. This is to confirm the previous modeling work showing that simple GCMs forced by constant heating reproduce observed mean climate (e.g. Hall 2000). As in the literature (e.g., Hoskins and Rodwell 1995), the low-level monsoon circulation over the Indian Ocean, as well as the subtropical high, is well reproduced

(Figs. 2a,d). Despite some discrepancies, such as a weak inflow to India, overrepresented westerly around the Philippines, and weak southerly off Peru, the overall features of the model climatology are sufficiently similar to the observations. Likewise, the upper-level zonal wind in the CLIM captures the observational feature showing the monsoon easterly in low latitudes, Pacific and Atlantic jets, and the split of the westerly cores over the eastern Pacific and Atlantic, except that the Pacific jet is too strong (Figs. 2b,e). The climatological mean fields in HIST are nearly identical to Figs. 2d,e, indicating that the interannual heating variability does not have a crucial role for reproducing *mean* climate (not shown).

In addition to the mean state, the variance distribution in the NLBM has to be realistic for the present purpose. The standard deviation (SD) of the observed low-frequency (longer than 10 days) geopotential height at 500 hPa (Z500) shows maxima over the North Pacific, northeastern parts of Canada and the Atlantic Ocean, and the Arctic region (Fig. 2c). The model counterpart underrepresents the amplitude, but the distribution closely resembles the observations (Fig. 2f). The variance distribution for the high-frequency Z500 is also compared; the model's similarity to nature is not as high as the low-frequency variance, but is acceptable for the Pacific and Atlantic storm tracks (not shown). Figure 2 thus reveals that the NLBM is capable of reproducing many aspects of the observed summer climatology, and is therefore worth using to analyze the fluctuations.

b. Potential predictability

The two sets of ensemble experiments, the CLIM and HIST, may be analogous to the AGCM experiments driven by the climatological and historical SSTs,

respectively. The latter, i.e., the AMIP experiment, is known to reveal the ensemble-mean signal produced by SST anomalies (e.g., Sugi et al. 1997). The signal-to-noise ratio of the forced variability can be measured by the potential predictability, *R*. Its definition is not unique (Pohlmann et al. 2004), but is commonly based on the ratio of the ensemble-mean variance to the total variance. Here, we follow the definition by Rowell et al. (1995):

$$R = \frac{\sigma_E^2 - \sigma_I^2 / n}{\sigma_T^2} \ , \tag{5}$$

where *n* denotes the ensemble size, σ_E^2 is the variance of the ensemble-mean quantity, σ_I^2 is the variance of the intra-ensemble deviations, and $\sigma_T^2 = \sigma_E^2 + \sigma_I^2$ represents the total variance. It should be noted that the second term of the numerator of (5) corrects the forced signal that is overestimated for insufficient ensemble size.

The potential predictabilities are calculated for the JJA-mean Z500 and the meridional wind at 200 hPa (V200) in the CLIM and HIST. As expected, *R* in the CLIM is quite low, roughly 10% or less for both Z500 and V200 (not shown). While the potential predictability in the CLIM, which is driven by the seasonally varying climatological heating, should, in principle, be zero, *R* has nonzero values because of the small sample size. In the HIST, *R* has high values of 80–90% over the low latitudes, and moderate values of 20–50% in the middle latitudes (Fig. 3). When compared with an AMIP-type AGCM experiment (cf. Fig. 5 of Sugi et al. 1997), the HIST provides higher potential predictability, probably due to the effect of the prescribed heating rather than the SST.

4. Circumglobal teleconnection

a. Detection of the variability

The NLBM experiments, which were driven by the monthly heating, provided global atmospheric fields that included a seasonal cycle. We analyzed the anomalies in both the winter and summer seasons, and confirmed that the model captured the dominant low-frequency variability in winter: the Pacific/North American pattern and the NAO (not shown). In this study, however, the purpose was to clarify the mechanisms that control the summer teleconnection patterns; therefore, the monthly anomalies during JJA were used for the subsequent analysis.

Following previous studies (Branstator 2002; Lu et al. 2002; Watanabe 2004), the monthly V200 anomaly is used to identify the CGT pattern. Since its major portion is observed around the Asian jet, an empirical orthogonal function (EOF) analysis is performed for V200 over the Eurasian region of 0° –150° E, 20° –60° N (Fig. 4). The leading EOF (EOF1) in the JRA reanalysis, accounting for 20.6% of the total variance, shows a wave-like pattern that originates over the North Atlantic and reaches far downstream to the North Pacific (Fig. 4a). The anomalies presented in Fig. 4a are the regression of V200 onto the principal component (PC) time series of the EOF1, and define the positive phase of the CGT in the present study. The CGT anomaly pattern is roughly out of phase with the V200 climatology (not shown), indicating that the Asian jet is relatively zonal in this phase. When compared to the winter CGT pattern (cf. Branstator 2002), the axis of the wave-like disturbances is shifted northward in accordance with the seasonal migration of the position of the climatological jet.

A similar EOF analysis of the V200 anomaly in the NLBM experiments results in the CGT pattern prevailing in the leading EOF (Fig. 4b,c). Except that the magnitude is roughly 75% of the observed EOF1, the spatial structure and the fractional variance

well resemble the observation shown in Fig. 4a. The ten members are not averaged, but simply combined, when calculating the covariance, so that the large sample size guarantees the robustness of the EOF pattern (the shading in Fig. 4b,c). It is noticeable that the CLIM and HIST have nearly identical CGT pattern. This indicates that the origin of the CGT lies in the internal dynamics of the summer extratropical circulation. Anomalies associated with the CGT in the other fields are obtained by means of the regression onto the PC time series of each EOF1; they are again similar among the reanalysis and the two experiments. Therefore, they are only shown for HIST (Fig. 5). Consistent with the V200 anomaly, the upper-tropospheric height anomaly reveals an ambient wave train from North America to East Asia (Fig. 5a). Some of their centers are accompanied by a surface signature, as presented in the sea-level pressure anomaly, which shows the anomalous low over the North Atlantic and eastern Europe and the anomalous highs over the Tibetan Plateau and Japan for the positive phase (Fig. 5b). The CGT pattern is roughly equivalent barotropic, but does accompany a low-level temperature anomaly (Fig. 5c). The 850 hPa winds show easterly anomalies over South Asia, suggesting that the monsoon westerly is weak and hence the summer monsoon activity is suppressed during the positive phase of the CGT (Fig. 5c).

The spatial structure of the CGT pattern is reminiscent of, and can be interpreted as, stationary Rossby waves trapped on the Asian jet (Hoskins and Ambrizzi 1993). Since the mean state does not favor a specific phase but only sets the possible wavenumber, the question of whether another CGT pattern exists with a different phase structure should be examined. In fact, the second EOFs (EOF2) for V200 also represent a wave-like pattern in quadrature with EOF1 in both the reanalysis and the two model experiments (not shown). Although the fractional variances of EOF2 are much smaller

than those of EOF1 (14.3, 13.5, and 14.8% for JRA, CLIM, and HIST, respectively), this fact indicates that the CGT can appear with various spatial phase structures.

The similarity of the EOFs in the CLIM and HIST may apparently indicate that the fluctuation in the heating does not affect the structure of the CGT. The EOF time series, however, indicate that the heating anomalies work to regulate its temporal behavior (Fig. 6). In the CLIM, there is no reason for any correspondence between the anomalies in each member and the observed anomaly. The interannual variability in each member is random and weakly correlated with the observations only by chance; therefore, the ensemble average has quite a small amplitude[1] and is almost independent of the observed EOF time series (Fig. 6a,b). In the HIST, all of the members show a positive correlation with the observations, so does the ensemble average (Fig. 6c,d). Indeed, the potential predictability of the CGT pattern, estimated as in section 3b but using the time series in Fig. 6c, reaches 39% in the HIST. The spatial distribution of R for V200 in the HIST reveals a wavy contour of R = 30% in the NH, and that the areas of high predictability coincide with the centers of the CGT pattern (thick contours in Fig. 3d).

In order to quantify the relationship between the heating anomaly and the CGT pattern in the HIST, a singular value decomposition (SVD) analysis is performed for the vertically-averaged heating, $\widehat{Q}$, and the ensemble-averaged V200 during summer. The resultant SVD1 represents the CGT pattern (Fig. 7a) and, as expected from Fig. 5c, there are negative anomalies in $\widehat{Q}$ over the Asian monsoon region (Fig. 7b). The amplitude of the V200 anomaly is roughly one third that of the EOF1, which is consistent with the value of R. The heating fields are somewhat noisy, but show a

[1] The ensemble mean should actually be zero for an ensemble of infinite size.

widespread heating anomaly over the eastern equatorial Pacific, northern tropical Atlantic, North America, and western equatorial Indian Ocean and a cooling anomaly over equatorial Africa and the monsoon area. The question of which of these heating and cooling anomalies is the most responsible for the CGT signal is further examined in section 4c.

b. Low-frequency CGT

It is known that an individual teleconnection pattern has a relatively short time scale (Feldstein 2000). On a daily basis, the CGT pattern has also been shown to have duration of about a week in winter and to not be completely stationary (Watanabe 2004). Therefore, the summer CGT is examined based on the daily anomaly fields that retain low-frequency (>10 days) components. This enables us to identify the source region of the wave train.

The daily CGT index is defined by the spatial projection of the low-frequency V200 anomaly on the EOF1 shown in Fig. 4. The characteristic time of the low-frequency CGT is first estimated by the autocorrelation function of the daily CGT indices (Fig. 8). The de-correlation time for the low-frequency CGT in JRA is about six days, which is similar to the persistence of the low-frequency variability in winter, e.g., NAO (Fig. 11 of Watanabe 2004). The duration of the simulated CGT is somewhat short: about 5 days (dashed curves in Fig. 8). The low-pass filter works to lengthen the de-correlation time (thin curves in Fig. 8); yet, the persistence of the low-frequency CGT indices are longer than that for the white noise to which the same low-pass filter was applied (not shown).

The composite evolution of the low-frequency CGT is constructed by referring

to the above index as a reference time series. For positive and negative phases, the daily anomalies are extracted when the index exceeds ±1 SD and is prolonged for more than 5 days. After the samples containing multiple peaks during one event of 11 days are discarded, composite maps are made with respect to the peak day of each event. Since the spatial structures of the composite CGT patterns were similar for the JRA and the two NLBM experiments, the lagged composites for the positive phase of the low-frequency CGT in the HIST, constructed from 297 events, are presented in Fig. 9; the sequence of figures indicates the evolution of the 200 hPa height and the associated wave activity flux (Takaya and Nakamura 2001) from 6 days before to 4 days after the peak.

At 6 days preceding the peak, the wave train is yet to be formed, but an anticyclonic anomaly dominates over the northeastern US and emanates wave energy eastward at around 50° N (Fig. 9a). The wave train grows over Eurasia during a few consecutive days, and even reaches Japan at day –2 (Fig. 9b,c). The pattern at the peak resembles the monthly anomaly (Fig. 5a) but appears more like a wave (Fig. 9d). After the peak, there is no energy propagation from the North Atlantic, whereas the anticyclonic anomalies over central Asia and west of Japan emanate wave energy southeastward and eastward, respectively, leading to the gradual decay (Fig. 9e,f). Lagged composites for the negative phase of the CGT are roughly the mirror to those in Fig. 9 (not shown). The low-frequency evolution is thus indicative of quasi-stationary Rossby waves, which have a clear life cycle; triggering and propagation over the North Atlantic; growth along the Asian jet; and decay over East Asia. Using the composite anomalies at 45° N, we estimated the zonal wavenumber (k), zonal phase speed (c_x), and group velocity (c_{gx}) of the low-frequency CGT as: $k \sim 5$, $c_x \approx 2.8$ m s^{-1}, and

$c_{gx} \approx 65$ m s^{-1}, respectively. The wavenumber is consistent with the observation in DW, and the CGT is thus slowly propagating. The eastward group velocity is slightly faster than that of stationary Rossby waves on a jet of about 25–30 m s^{-1}. This inconsistency may not be surprising because the CGT is not a neutral Rossby wave, but is accompanied by energy conversion with the background mean state, as discussed below.

The climatological westerlies have a double core over the North Atlantic (Fig. 2e and the shading in Fig. 11a). The wave packets triggering the CGT come along the Atlantic jet, where the eddy has a meridionally elongated shape around the jet exit, which means that barotropic energy conversion gives up energy to the background flow. However, we found a divergence of the wave activity flux to the west of the British isles from day –4 to day –2, suggesting that the baroclinic conversion is responsible for the emission of wave energy at around 10° W, 50° N (Fig. 9b,c). It is evident that the cyclonic and anticyclonic eddies over Eurasia are tilted in the southwest-northeast direction throughout the life cycle. With reference to the latitude of the mean jet of about 40° N, the eddies before the peak are located to the north, which are preferable for gaining energy from the background state through the barotropic conversion term $-\tilde{u}\tilde{v}\partial U/\partial y$, where the chide denotes the low-frequency anomaly and U is the climatological zonal wind (shading in Fig. 9b,c, and also positive sign of the area-averaged conversion term). As the wave energy propagates eastward and southeastward, eddies eventually end up on the equatorward side of the jet, leading to the sign reversal of the barotropic conversion and consequently the gradual decay of the CGT after day +2 (Fig. 9e,f).

Since the heating fields have only the monthly or longer time scale, it is not obvious how the low-frequency CGT as shown in Fig. 9 is related with the forced CGT

signal obtained from the SVD analysis (cf. Fig. 7a). One possible interpretation is that the monthly anomalies associated with the CGT presented in section 4a are indicative of the change in the frequency of occurrence of the low-frequency (intraseasonal) states. In order to examine this, the probability density function (PDF) of the daily low-frequency anomalies in the HIST is calculated on a two-dimensional plane spanned by the leading two EOFs for V200 (cf. Fig. 4c). Specifically, time series obtained by projecting the daily V200 anomaly onto the EOFs are plotted in the phase space, and then the PDF is estimated following Mori and Watanabe (2008). Note that although orthogonality between the two time series is not guaranteed, they are actually nearly orthogonal (the correlation is 0.063).

The PDF using all the samples of 26680 days roughly reveals a Gaussian structure (not shown). Change in the frequency of occurrence of the low-frequency CGT is then evaluated by comparing that PDF and the PDFs using the sub-samples when the SVD expansion coefficients for $\widehat{Q}$ are either above +0.5 SD or below –0.5 SD (Fig. 10a,b). The deviations of the PDFs (shading in Fig. 10) clearly show that the heating anomaly associated with the SVD1 systematically changes the PDFs, mainly along the EOF1 axis; a positive (negative) low-frequency CGT occurs more frequently for a positive (negative) $\widehat{Q}$. The mean position of the trajectory, marked by plus sign, is very close to the origin as compared with the range of the low-frequency CGT. This apparently indicates some role of nonlinearity in the forced CGT signal. However, the values of skewness are 0.45 and 0.52 for the positive and negative phases, which are not systematically different from the skewness of the mean PDF (0.47); therefore the change in the PDF mostly arises from the shift of the mean position but not the change in its shape (Fig. 10c,d). The PDFs shown in Fig. 10 are thus interpreted as a linear

superposition of the forced monthly anomaly on the low-frequency component. In the next section, we demonstrate that the monthly CGT anomaly is indeed directly driven by the monthly heating anomaly, rather than being a consequence of the modified frequency occurrence of the low-frequency variability.

c. Forcing processes of the CGT

The SVD1 for the ensemble-mean V200 and $\widehat{Q}$ (Fig. 7) exhibits the forced CGT signal in the HIST. Since the $\widehat{Q}$ anomalies in Fig. 7b spread over a wide area, we tried to identify which part of the heating anomaly was responsible for exciting the CGT pattern. For this purpose, the linearized version of the NLBM, i.e., the LBM (cf. section 2c), was used to calculate the steady response forced by the SVD1-related heating anomaly, which was obtained from the linear regression of the 3D heating anomaly upon the expansion coefficients for $\widehat{Q}$. The steady response was obtained by simply integrating the LBM for 100 days, and averaging the last 20 days. This is a reasonable approximation to the steady response since the anomaly fields little change after 20-30 days.

Prior to presenting the steady response, the change in the storm tracks associated with the SVD1 is also examined because of a possibility that the relationship between the circulation anomaly and the heating variability involves feedbacks from transients. The high-frequency transients are defined by the residual between the raw daily and low-pass filtered data, and the storm track is measured by the root-mean-square of the 500 hPa height in JJA, denoted as $\sqrt{\overline{Z'^2}}$, where the prime indicates the high-frequency quantity and the over bar denotes the monthly mean. The storm activity during the

summertime is weaker than that during winter, and its variability is also weak. Yet, the monthly anomaly of the ensemble mean $\sqrt{\overline{Z'^2}}$ associated with the SVD1 shows that the storm track in the HIST is systematically intensified (Fig. 11). Therefore, the heat and vorticity forcing terms due to transients, $-\nabla\bullet(\overline{\mathbf{v}'T'})$ and $-\nabla\bullet(\overline{\mathbf{v}'\varsigma'})$, averaged for all the members, are calculated, and the anomalous eddy forcing is given to the LBM in a similar manner to the diabatic heating.

The steady V200 response to the sum of the diabatic heating anomaly and the anomalous transient eddy forcing is shown in Fig. 12a, which is sufficiently comparable to the SVD pattern in Fig. 7a, except for the latitude and amplitude of the response around Greenland. The effective beta, a measure of the waveguide in the basic state, reveals maxima associated with the Atlantic and Asian jets (shading), and the stationary wave response occurs on these waveguides. The low-level temperature and wind anomalies associated with the SVD1 (not shown, but quite similar to Fig. 5c) are also well reproduced by the LBM (Fig. 12b). It should be emphasized that the CGT pattern is reproduced in terms of the structure and amplitude mostly by the diabatic heating and the effect of transients is negligible (Fig. 12c,d). This indicates that the eddy-mean flow interaction is of secondary importance in the summertime CGT. We confirmed that the LBM employing the summer climatology derived from JRA-25 also produced a wavy steady response to the same heating anomaly (not shown).

Given that the LBM is capable of reproducing the anomaly patterns in the HIST, the heating anomaly is decomposed into 11 regions following the $\widehat{Q}$ anomaly pattern (Fig. 13a). The steady V200 response to the sum of the heating over these regions does represent the CGT-like pattern quite similar to Fig. 12c, so that these 11 regions cover

most of the diabatic forcing crucial to the forced CGT signal (Fig. 13b). In order to clarify which of the regional heating anomalies is the most responsible to the total response, the steady V200 response to each of the regional heating (labeled from A to K in Fig. 13) was projected on to the V200 response shown in Fig. 13b over Eurasia in the box 0° –150° E, 20° –60° N. The relative contribution of the regional heating to the CGT pattern is then presented by the fractional variance and the spatial correlation coefficients (Fig. 13c).

The most noticeable feature in Fig. 13c is that the heating in region K, from the East Mediterranean Sea to the Caspian region, explains 60% of the total response. Since the CGT pattern over Eurasia starts growing around the Asian jet entrance region (Fig. 9), the large sensitivity of the response to the heating in this region is reasonable, and suggests that the prediction of precipitation anomaly in the East Mediterranean Sea is the key for better forecasting the CGT pattern. However, care must be paid to interpret the cause and effect when the forcing is in the vicinity of the response. The LBM solves balance equations, so that the heating anomaly in the region K might result from the CGT pattern that accompanies the low-level southerly anomaly (Fig. 12b). Interaction processes between the CGT pattern and the East Mediterranean heating, if any, cannot be elaborated in the present analysis, and remain the future issue. Similarly, the V200 response to the diabatic cooling anomaly in the Asian monsoon region (region E) is highly correlated with the total response (r=0.64). While this anomalous cooling may also represent a feedback from the summer monsoon precipitation as suggested by DW, its contribution to the total CGT response is less than 10%; therefore the coupling between the CGT and monsoon appears to be of secondary importance.

In addition to the heating anomalies near the CGT pattern, there are two remote

regions that significantly contribute to the total response: regions C (equatorial Africa) and I (North America), which explain 18% and 17% of the total variance, respectively. The time evolution of the response illustrates that these regional heating anomalies excite the CGT-like response in a different manner (not shown). The diabatic cooling anomaly over equatorial Africa induces an upper-level convergence, and the anomalous northerly crossing the Asian jet over northern Africa generates the Rossby wave source. Consequently, the stationary wave train is formed downstream along the Asian jet. On the other hand, the diabatic heating anomaly over US excites the wave train along the Atlantic jet. The waves having the meridional scale larger than the distance between the Atlantic and Asian jets seem to overcome the potential vorticity barrier over the eastern Atlantic, and extend further downstream along the Asian jet. This is indeed found in the evolution of the low-frequency CGT (Fig. 9).

The results shown in Fig. 13 leads to the following interpretation to the forcing mechanism of the CGT: the forced CGT signal is primarily excited by the remote heating in equatorial Africa and in the midlatitude US mainland, and the low-level circulation anomaly associated with the CGT in turn intensifies the precipitation over the East Mediterranean region, which is actually the major driver of the CGT response. This scenario is different from that proposed by DW; the reason is discussed in the next section.

The LBM diagnoses suggest that the remote diabatic heating favors a particular phase of the CGT pattern. It is therefore worth examining whether the heating anomaly, as shown in Fig. 7b, is induced by slow SST changes. If so, then there may be prospects for predicting this aspect of CGT variability. Figure 14 illustrates the regression of the summer SST anomalies upon the SVD expansion coefficients for $\widehat{Q}$. Significant SST

anomalies are found in the Pacific, North and South Atlantic, and the western Indian Ocean. The Pacific SST anomalies are reminiscent of El Niño, whereas the positive SST anomaly in the northwestern Indian Ocean is likely a response of the ocean mixed layer to the weakened low-level monsoon circulation.

It is straightforward to investigate the relationship between $\widehat{Q}$ and El Niño, the latter represented by the Niño 3 SST anomalies. Instead of using the SVD expansion coefficients (Fig. 7c), we expand the monthly JJA $\widehat{Q}$ anomaly fields in the EOFs, onto which the SVD pattern in Fig. 7b is projected (Fig. 15). The fractional variance and the correlation with the Niño 3 index are also considered. It is found that EOF1 for $\widehat{Q}$, which accounts for 14.2% of the total variance, is strongly correlated with the Niño 3 index (r = 0.85). However, the spatial pattern that reveals an east-west seesaw in the tropical Pacific (not shown) is distinct from the SVD1 for $\widehat{Q}$, as indicated by the negligible projection coefficient in Fig. 15. The SVD pattern has a considerable projection onto EOF2, which is only weakly correlated with El Niño (r = 0.31). In short, the optimal heating anomaly pattern, i.e., SVD1, for the CGT is not directly related to El Niño. There is a possibility that the optimal heating pattern has a lagged relationship with ENSO. However, this is beyond the scope of this study, and will be clarified in future work.

5. Summary and discussion

In the present study, possible forcing mechanisms for the dominant teleconnection pattern during the NH summer season, i.e., the CGT, were examined by means of numerical experiments based on a dry AGCM. The dry AGCM, called the

NLBM throughout this study, was driven by the monthly diabatic heating, either including or excluding the interannual fluctuations from 1979 to 2004. We performed two sets of ensemble experiments: one with climatological heating (CLIM) and the other with historical heating (HIST). The long-term mean fields obtained from the NLBM well captured the observed summer climatology. High potential predictability was found in the HIST, arising from the prescribed anomalies in diabatic heating.

Following previous studies, we identified the CGT pattern by analyzing V200 anomalies during JJA. The CGT revealed wave packets over Eurasia; the phase structures seen in observation and the two model experiments were nearly identical, indicating that the origin of the CGT should be explained by the internal dry dynamics of the atmosphere. On the other hand, the ensemble mean of the CGT had a potentially predictable signal in the HIST.

The forcing mechanism and optimal diabatic heating anomaly of the CGT were then investigated using the LBM. The steady linear response to the heating anomaly associated with the CGT as found in the HIST closely resembled the CGT simulated in the NLBM. Further diagnoses demonstrated that the forced CGT signal was largely generated by the anomalous heating over the East Mediterranean Sea and Caspian region, which correspond to the area of the Asian jet entrance. The CGT response accompanies the anomalous low-level southerly over these areas, suggesting that the CGT is coupled with the local heating over the East Mediterranean region. In addition, remote heating anomalies also worked to create the CGT-like response; in particular, the heating anomalies over North America and the cooling anomaly over equatorial Africa were found to be effective in exciting stationary Rossby waves trapped on the Atlantic and Asian jets, respectively. The forced CGT signal was also accompanied by a

cooling anomaly in the Asian monsoon region, which may arise from a coupling between the CGT and the Asian summer monsoon, but it is not the leading mechanism of the forced CGT signal.

The positive (negative) phase of the CGT pattern, following the definition in this study (cf. section 4a), corresponds to the zonal (wavy) Asian jet, which is associated with weak (strong) monsoon activity, as revealed from the concurrent heating anomaly (Fig. 7b). This relationship may be consistent with the finding by Enomoto et al. (2003) and Enomoto (2004), who showed that the adiabatic descent to the northwest of the Indian summer monsoon heating acts as a wave source and thereby causes the wavy Asian jet. One difference is that their "silk road" pattern was detected in August, while the CGT pattern in this study was the variability that was dominant throughout the boreal summer season. The anomalous cooling around Japan may thus represent the weakened Baiu-Changma front but not the anomalous weather in mid-summer.

The forcing mechanism of the summer CGT, as summarized in section 4c, is qualitatively different from that proposed by DW, who speculated that the heating anomaly associated with the Indian summer monsoon variability links the wave trains propagating from Europe and to East Asia. In our diagnosis, the monsoon heating anomaly contributes some to the forced CGT response, but is not of importance (Fig. 13c). Furthermore, DW did not identify the remote forcing of the CGT because it can only be detected in the ensemble of the model experiments, as in this study. There are thus differences between DW and our study, in terms of the approach (data analysis and modeling) and the analysis method; the most relevant difference may be the definition of the CGT, as discussed below.

In DW, the CGT was identified by one-point correlation maps and the leading EOF for the monthly 200 hPa geopotential height (Z200). We also used the JRA-derived Z200 anomaly to obtain an EOF that is quite similar to DW's EOF1. The spatial pattern includes, as was shown in DW, a large zonally uniform component (their Fig. 4). The V200 anomaly associated with this EOF does show the CGT, but with amplitude smaller than Fig. 4a. Indeed, the correlation between the PCs of the V200 and Z200 EOFs only reaches 0.27, which is marginally significant. This implies that the EOF1 for Z200 is contaminated by fluctuations not associated with the CGT. It has been reported that zonally elongated variability dominates in Z200, which is forced by an ENSO-like tropical SST anomaly (e.g., Schubert et al. 2002). The heating anomaly that forces the CGT identified in the present study is not strongly related to ENSO (cf. Fig. 14); therefore, an analysis using the geopotential height fields may result in a mixture of the CGT and the atmospheric response to El Niño. This is consistent with DW's results showing a subtle relationship among the CGT, monsoon, and ENSO.

One implication of this study is that the forcing mechanism of the summertime CGT that is largely generated by internal dynamics and partly controlled by tropical diabatic heating variability is hardly identified from observations, which is one realization of nature. A key finding in this study will therefore be the detection of an optimal heating pattern for the CGT (cf. Fig. 8). For a more robust conclusion, it would be worth examining the relationship between the CGT and heating anomalies in AMIP-type AGCM experiments. In addition, the predictability of the heating pattern shown in Fig. 7b and the oceanic conditions for its occurrence are issues that remain to be investigated, and may be elucidated by extensively using the products of the ensemble seasonal forecast.

Acknowledgments. The authors thank Steven Feldstein, Hisashi Nakamura, and two anonymous reviewers for useful comments. Thanks are also due to Masato Mori, who helped calculating the 2D PDF. This work was partly supported by a Grant-in-Aid for Scientific Research from MEXT, Japan.

APPENDIX

Linearized scheme for turbulent diffusion

The conventional LBM adopts a horizontally uniform drag at low levels in order to prevent the growth of unstable baroclinic waves. Such a linear drag would, however, be too crude to approximate the boundary layer diffusion that works to stabilize the system locally. A better approach is to linearize a turbulent closure scheme to represent the boundary layer dissipation.

Above the surface layer, the turbulent fluxes of anomalous momentum and heat are evaluated with the Yamada-Mellor level 2.0 closure in our model. Let either variable of the above components be X',

$$\frac{dX'}{dt} = \frac{\partial}{\partial \sigma}\left(\bar{K} \frac{\partial X'}{\partial \sigma} \right), \tag{A1}$$

where

$$K = f(R_i)$$

is the vertical mixing coefficient determined as a function of the Richardson number, $R_i = \left(g\theta_s^{-1} \partial\theta / \partial z \right) / \left(\partial^2 u / \partial z^2 + \partial^2 v / \partial z^2 \right)$. The over bar denotes the basic state quantity, and the perturbation of K is ignored in (A1). Because of nonlinearity in f, we can

approximate $\overline{R_i(X)} \simeq R_i(\overline{X})$, but $\overline{K(R_i)} \neq K(\overline{R_i})$. Therefore, we assume a PDF for R_i; its variance is determined from an empirical relationship found in the CCSR/NIES/FRCGC AGCM.

$$\sigma_{R_i} = \begin{cases} r^+ \overline{R_i}\left(1 - \sqrt{\overline{R_i} / R_i^{\max}}\right) & \text{for} \quad \overline{R_i} > 0 \\ r^- \overline{R_i} & \text{otherwise} \end{cases}, \tag{A2}$$

where $r^+ = 2.40$, $r^- = -0.99$, and $R_i^{\max} = 100$.

Since a shear term in R_i may bring a skewed probability distribution, we employ a beta function for the basis of the PDF:

$$G(y) = \frac{1}{B(p,q)} \frac{(y-a)^{p-1}(b-y)^{q-1}}{(b-a)^{p+q-1}} \quad \text{for} \quad a \le y \le b, \tag{A3}$$

where

$$B(p,q) = \frac{\Gamma(p)\Gamma(q)}{\Gamma(p+q)},$$

and the first three moments are given as follows.

$$\overline{y} = (b-a)\frac{p}{p+q} + a \ , \ \sigma_y = \frac{b-a}{p+q}\sqrt{\frac{pq}{p+q+1}} \ , \ S_y = \frac{2(q-p)}{p+q+2}\sqrt{\frac{p+q+1}{pq}}$$

In the present application, we ignore the skewness parameter for simplicity, so that $p = q$ and the PDF can be determined with the variance and a half-width Δy as

$$p = \frac{1}{2\sigma_y^2}\left(\Delta y^2 - \sigma_y^2\right), \tag{A4}$$

where

$$\Delta y = \begin{cases} 1 - \overline{y} & \text{for} \quad \overline{y} > 0.5 \\ \overline{y} & \text{otherwise} \end{cases}.$$

The lower and upper bounds of the PDF are simply $a = \overline{y} - \Delta y$ and $b = \overline{y} + \Delta y$.

Now R_i is projected on to y as $y = (R_i + R_i^{\max})/2R_i^{\max}$, so that $-R_i^{\max} \le \overline{R_i} \le R_i^{\max}$ corresponds to $0 \le y \le 1$. Likewise, the variance σ_{R_i} can be projected on to σ_y, and then the dimensional function for the PDF becomes

$G^*(R_i) = R_i^{\max}\left[2G(y) - 1\right]$ for $R_i^- \le R_i \le R_i^+$.

The basic state mixing coefficient $\overline{K}$ is finally calculated as

$$\overline{K} = \int_{R_i^-}^{R_i^+} f(R_i) G^*(R_i) dR_i \Bigg/ \int_{R_i^-}^{R_i^+} G^*(R_i) dR_i \,. \qquad \text{(A5)}$$

In Fig. A1, we compare $\overline{K}$ for momentum, calculated using (A5), and the climatological mean value of the momentum mixing coefficients in the CCSR/NIES/FRCGC AGCM. Despite the difference in the small-scale feature, the above linear approximation is shown to capture the overall magnitude and distribution of the mean mixing coefficients, especially those over the western sides of the northern extratropical oceans where weak stratification leads to strong vertical mixing. These regions correspond to the primary baroclinic zone, so that linear diffusion (A1) with the basic state mixing coefficient shown in Fig. A1b effectively suppresses the baroclinic instability without damping larger scale perturbation.

The steady linear response is known to be sensitive to the dissipation term, in particular the linear drag in the boundary layer. The linearized turbulent closure automatically determines the strength of the boundary layer damping depending on the basic state, so that the scheme largely reduces arbitrariness for the dissipation process in the linearized model, although a similar pattern of the forced response may be obtained with conventional linear drag when the coefficients are carefully tuned.

REFERENCES

Ambrizzi, T., B. J. Hoskins, and H.-H. Hsu, 1995: Rossby wave propagation and teleconnection patterns in the Austral winter. *J. Atmos. Ssci.*, **52**, 3661-3672.

Branstator, G., 2002: Circumglobal teleconnections, the jet stream waveguide, and the North Atlantic Oscillation. *J. Climate*, **15**, 1893-1910.

Ding, Q., and B. Wang, 2005: Circumglobal teleconnection in the Northern Hemisphere summer. *J. Climate*, **18**, 3483-3505.

Enomoto, T., B. J. Hoskins, and Y. Matsuda, 2003: The formation mechanism of the Bonin high in August. *Quart. J. Roy. Meteor. Soc. Japan*, **129**, 157-178.

Enomoto, T., 2004: Interannual variability of the Bonin high associated with the propagation of Rossby waves along the Asian jet. *Quart. J. Roy. Meteor. Soc. Japan*, **82**, 1019-1034.

Feldstein, S. B., 2000: The timescale, power spectra, and climate noise properties of teleconnection patterns. *J. Climate*, **13**, 4430-4440.

Gates, W. L., and Co-authors, 1999: An overview of the results of the Atmospheric Model Intercomparison Project (AMIP I). *Bul. Amer. Meteor. Soc.*, **80**, 29-55.

Hall, N. M., 2000: A simple GCM based on dry dynamics and constant forcing. *J. Atmos. Sci.*, **57**, 1557-1572.

Held, I. M., and M. J. Suarez, 1994: A proposal for the Intercomparison of the dynamical cores of atmospheric general circulation models. *Bul. Amer. Meteor. Soc.*, **75**, 1825-1830.

Hoskins, B. J., and T. Ambrizzi, 1993: Rossby wave propagation on a realistic longitudinally varying flow. *J. Atmos. Ssci.*, **50**, 1661-1671.

Hoskins, B. J., and M. J. Rodwell, 1995: A model of the Asian summer monsoon. *J. Atmos.*

Sci., **52**, 1329-1340.

Hsu, H.-H., and S.-H. Lin, 1992: Global teleconnections in the 250-mb streamfunction field during the Northern Hemisphere winter. *Mon. Wea. Rev.*, **120**, 1169-1190.

Kosaka, Y., H. Nakamura, M. Watanabe, and M. Kimoto, 2009: Analysis on the dynamics of a wave-like teleconnection pattern along the summertime Asian jet based on a reanalysis dataset and climate model simulations. *J. Meteor. Soc. Japan*, **87**, in press.

Krishnan, R., and M. Sugi, 2001: Baiu rainfall variability and associated monsoon teleconnections. *J. Meteor. Soc. Japan*, **79**, 851-860.

Lau, K.-M., K.-M. Kim, and J.-Y. Lee, 2004: Interannual variability, global teleconnection and potential predictability associated with the Asian summer monsoon. *East Asian Monsoon*, C.-P. Chang, Ed., World Scientific, 564pp.

Lin, H., G. Brunet, and J. Derome, 2007: Intraseasonal variability in a dry atmospheric model. *J. Atmos. Ssci.*, **64**, 2422-2441.

Louis, J., 1979: A parametric model of vertical eddy fluxes in the atmosphere. *Bound.-Layer Meteor.*, **17**, 187-202.

Lu, R.-Y., J.-H. Oh, and B.-J. Kim, 2002: A teleconnection pattern in upper-level meridional wind over the North African and Eurasian continent in summer. *Tellus*, **54A**, 44-55.

Mellor, G. L., and T. Yamada, 1982: Development of a turbulence closure model for geophysical fluid problems. *Rev. Geophys. Space Phys.*, **20**, 851-875.

Mori, M., and M. Watanabe, 2008: The Growth and Triggering Mechanisms of the PNA: A MJO-PNA Coherence. *J. Meteor. Soc. Japan*, **86**, 213-236.

Onogi, K., and Co-authors, 2007: The JRA-25 Reanalysis. *J. Meteor. Soc. Japan*, **85**, 369-432.

Pan, L.-L, F.-F Jin, and M. Watanabe, 2006: Dynamics of synoptic eddy and low-frequency

flow interaction. Part III: Baroclinic model results. *J. Atmos. Sci.*, **63**, 1709-1725.

Peterson, K. A., R. J. Greatbatch, J. Lu, H. Lin, and J. Derome, 2002 : Hindcasting the NAO using diabatic forcing of a simple AGCM. *Geophys. Res. Lett.*, **29**, 1336–1339.

Pohlmann, H., M. Botzet, and M. Latif, 2004: Estimating the decadal predictability of a coupled AOGCM. *J. Climate*, **17**, 4463-4472.

Rayner, N. A., and Co-authors, 2003: Global analyses of sea surface temperature, sea ice, and night marine air temperature since the late nineteenth century. *J. Geophys. Res.*, 108, doi:10.1029/2002JD002670.

Rowell, D. P., C. Folland, K. Maskell, and M. N. Ward, 1995: Variability of summer rainfall over tropical north Africa (1906-92): Observations and modeling. *Q. J. Roy. Meteor. Soc.*, **121**, 669-704.

Sardeshmukh, P. D., and P. Sura, 2007: Multiscale impacts of variable heating in climate. *J. Climate*, **20**, 5677-5695.

Schubert, S. D., M. J. Suarez, P. J. Pegion, and M. A. Kistler, 2002: Predictability of Zonal Means during Boreal Summer. *J. Climate*, **15**, 420-434

Sugi, M., R. Kawamura, and N. Sato, 1997: A study of SST-forced variability and potential predictability of seasonal mean fields using the JMA global model. *J. Meteor. Soc. Japan*, **75**, 717-736.

Takaya, K., and H. Nakamura, 2001: A formulation of a phase-independent wave-activity flux for stationary and migratory quasigeostrophic eddies on a zonally varying basic flow. *J. Atmos. Sci.*, **58**, 608-627.

Terao, 1998: Barotropic disturbances on intraseasonal time scales observed in the midlatitudes over the Eurasian continent during the northern summer. *J.Meteor. Soc. Japan*, **76**, 419-436.

Trenberth, K. E., and L. Smith, 2008: Atmospheric energy budgets in the Japanese

reanalysis: evaluation and variability. *J.Meteor. Soc. Japan*, **86**, 579-592.

Watanabe, M., and M. Kimoto, 2000: Atmosphere-ocean thermal coupling in the North Atlantic: A positive feedback. *Quart. J. R. Met. Soc.*, **126**, 3343-3369.; Corrigendum. *Quart. J. R. Met. Soc.*, **127**, 733-734.

Watanabe, M., and F.-F. Jin, 2004: Dynamical prototype of the Arctic Oscillation as revealed by a neutral singular vector. *J. Climate*, **17**, 2119-2138.

Watanabe, M., 2004: Asian jet waveguide and a downstream extension of the North Atlantic Oscillation. *J. Climate*, **17**, 4674-4691.

Watanabe, M., 2009: Self-limiting feedback between baroclinic waves and a NAO-like sheared zonal flow. *Geophys. Res. Lett.*, **36**, doi:10.1029/2009GL037176.

FIGURE CAPTIONS

Fig.1 Climatological mean of the vertically averaged diabatic heating, $\widehat{Q}$, in the boreal summer. The unit is K dy^{-1} and the contour interval is 1 K dy^{-1}.

Fig.2 Climatological mean states in JJA derived from JRA-25: (a) SLP (contour; hPa) and 850hPa winds (vector; m s^{-1}), (b) 200 hPa zonal wind (contour interval 5 m s^{-1}), and (c) standard deviation for the low-frequency anomalies in Z500 (contour interval 5 m). (d)-(f) As in (a)-(c) but for the 10-member ensemble average of the CLIM experiment.

Fig.3 Potential predictability in HIST for (a) Z500 and (b) V200 in JJA. The contour interval is 10%. The thick contour in (b) indicates the ± 1 m s^{-1} isoline for the V200 EOF shown in Fig. 4c.

Fig.4 Leading EOFs to V200 in JJA during 1980-2004: (a) JRA25, (b) CLIM, and (c) HIST, as presented by the linear regression of V200 anomalies on to the associated PC time series. The EOF is performed over the Eurasian region of 0° –150° E, 20° –60° N (thick rectangle in (a)). The unit is m s^{-1} and the contour interval is 0.5 m s^{-1} exceeding ± 1 m s^{-1}. The shading indicates the anomaly significant at the 95% level.

Fig.5 Monthly anomalies of (a) 300 hPa geopotential height (contour interval 5 m), (b) SLP (contour interval 0.2 hPa), and (c) temperature (contour; interval 0.1 K) and winds (vector) at 850 hPa, regressed upon the PC time series associated with the V200 EOF1 in the HIST. The shading indicates anomalies significant at the 99% level.

Fig.6 (a) PC time series of the EOF1 for V200 in the CLIM. The PCs for each member

are shown by thin curves, and the ensemble mean and its 1 SD are indicated by the thick white curve and shading. (b) Correlation coefficients of the PC time series for each member in (a) with that in JRA. (c)-(d) As in (a)-(b) but for the HIST.

Fig.7 Leading SVD to monthly anomalies of V200 and $\hat{Q}$ in JJA during 1980–2004: heterogeneous regression for (a) V200 and (b) $\hat{Q}$, and (c) the expansion coefficients. The domain is the same as the EOF for V200 but is global for $\hat{Q}$. Note that the V200 anomalies are the ensemble average. The contour interval is 0.3 m s^{-1} in (a) and 0.1 K day^{-1} in (b), and the shading indicates the anomaly significant at the 95% level.

Fig.8 Autocorrelation functions for the low-frequency CGT index in JRA (solid), CLIM (dotted), and HIST (dashed). Autocorrelations for the unfiltered daily indices are also shown by thin curves. The crossing point between them and the horizontal thin line indicates the de-correlation time.

Fig.9 Time evolution of the composite low-frequency anomalies of the 200 hPa geopotential height (contour; interval 20 m) and the wave activity fluxes (vector) associated with the CGT pattern in HIST from (a) lag –6 days to (f) lag +4 days. Shown by shading is the barotropic energy conversion concurrent with the respective anomaly field. The energy conversion term averaged over 0°-150° E, 20° -60° N is also indicated at the bottom right of each panel.

Fig.10 2D PDF for the low-frequency V200 anomalies (contour; interval 0.02) in JJA over the Eurasian region of 0° –150° E, 20° –60° N in the HIST, using samples when the SVD expansion coefficients for $\hat{Q}$ (Fig. 7c) are (a) above 0.5 SD and (b) below –0.5 SD. The shading represents the deviation of the PDF from that

calculated with all the available samples. The time-mean anomaly states are indicated by crosses. (c)-(d) As in (a)-(b) but for the 1D PDF along the PC1 axis (thick curve) superimposed on the PDF using all the samples (thin curve).

Fig.11 Anomalies of the storm track, $\sqrt{\overline{Z'^2}}$, at 500 hPa in the HIST (contour) regressed on the expansion coefficients associated with the SVD1. The contour interval is 0.2 m, and the anomalies significant at the 95 % level are shown by thick contours. The shading indicates the JJA climatology of $\sqrt{\overline{Z'^2}}$ at 500 hPa.

Fig.12 Steady linear response in (a) V200 (contour interval 0.3 m s^{-1}) and (b) temperature (contour; interval 0.1 K) and winds (vector) at 850 hPa to the sum of the anomalous diabatic heating and the high-frequency eddy forcing both associated with the SVD shown in Fig. 7b. (c)-(d) As in (a) but for the responses to the heating and the eddy forcing, respectively. The basic state is derived from the JJA climatology in HIST, and the shading in (a) indicates the effective beta of the basic state exceeding 3×10^{-11} m^{-1} s^{-1}. Supplemental contours (interval 0.1 m s^{-1}) are shown by thin lines in (d).

Fig.13 (a) Regional division of the diabatic forcing given to the LBM (boxes labeled from A to K) superimposed on $\hat{Q}$ (shading, same as Fig. 7b). (b) As in Fig. 12c but for the response to the sum of the forcing over the 11 regions defined in (a). (c) Fractional variance (bars) and spatial correlation (curve) of the V200 response to each regional forcing with that shown in (b), evaluated over Eurasia of 0°-150° E, 20° -60° N.

Fig.14 Monthly anomalies of SST in JJA regressed upon the SVD expansion coefficients for $\hat{Q}$. The contour interval is 0.1 K and the shading indicates the

anomalies significant at the 95% level.

Fig.15 Fractional variance of the EOF (curve with circles) for monthly $\hat{Q}$ in JJA over the tropics of 30° S–30° N, correlation between the PC time series and the Niño 3 SST anomaly (dashed curve), and the spatial projection coefficients of the SVD1 for $\hat{Q}$ (Fig. 7b) on to the EOF patterns (bars). The projection only measures the similarity of the horizontal structure, so that the sign of eigenvectors are reversed if the projection is negative.

Fig. A1 The vertical diffusion coefficients for momentum at σ=0.98, obtained from (a) the climatology in the AGCM and (b) linearized turbulence closure in the LBM. The contour interval is 20 m^2 s^{-1}, and the values above 60 m^2 s^{-1} are indicated by the thick contour.

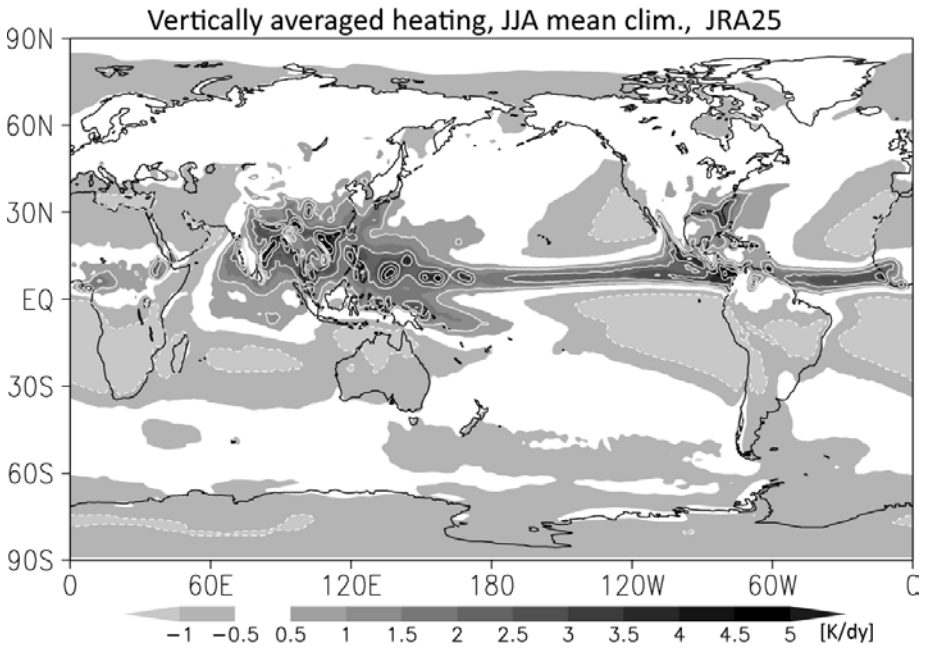

Fig.1 Climatological mean of the vertically averaged diabatic heating, $\widehat{Q}$, in the boreal summer. The unit is K dy^{-1} and the contour interval is 1 K dy^{-1}.

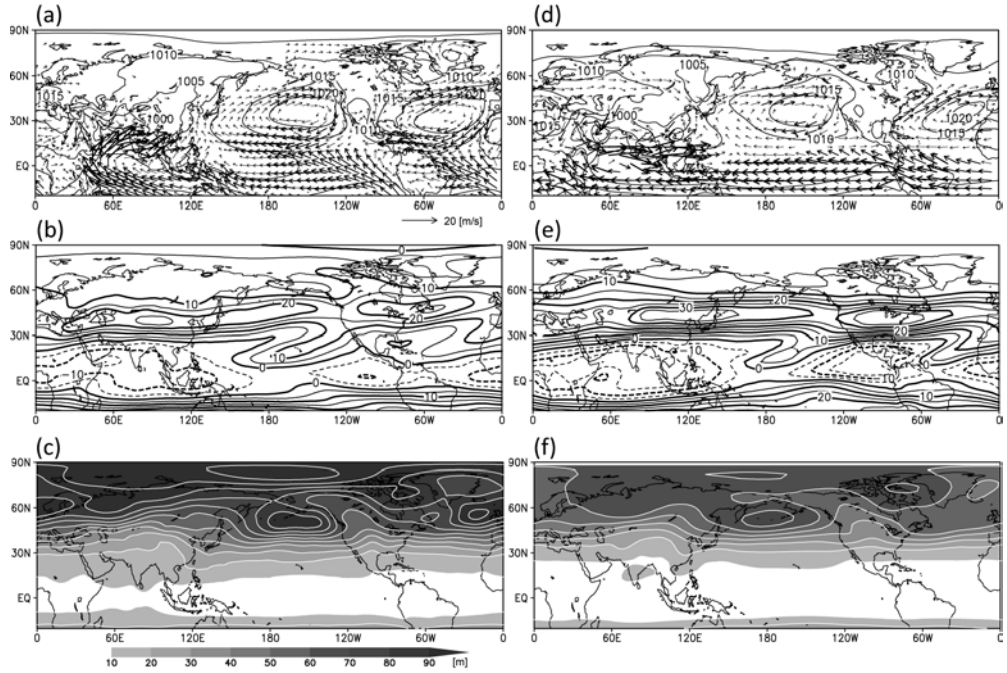

Fig.2 Climatological mean states in JJA derived from JRA-25: (a) SLP (contour; hPa) and 850hPa winds (vector; m s^{-1}), (b) 200 hPa zonal wind (contour interval 5 m s^{-1}), and (c) standard deviation for the low-frequency anomalies in Z500 (contour interval 5 m). (d)-(f) As in (a)-(c) but for the 10-member ensemble average of the CLIM experiment.

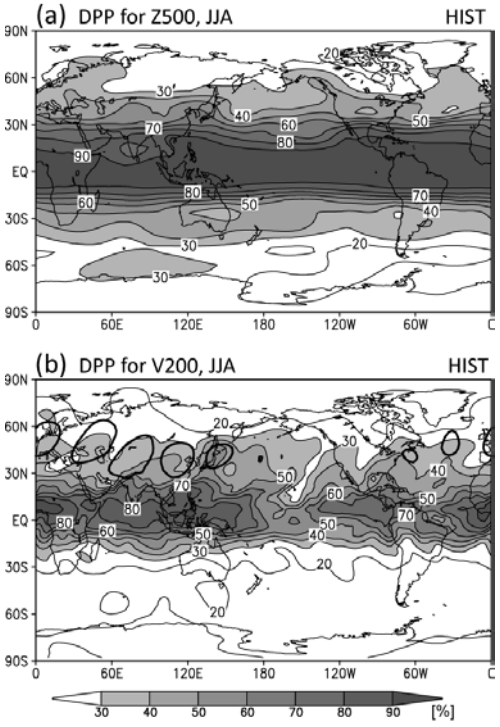

Fig.3 Potential predictability in HIST for (a) Z500 and (b) V200 in JJA. The contour interval is 10%. The thick contour in (b) indicates the ± 1 m s^{-1} isoline for the V200 EOF shown in Fig. 4c.

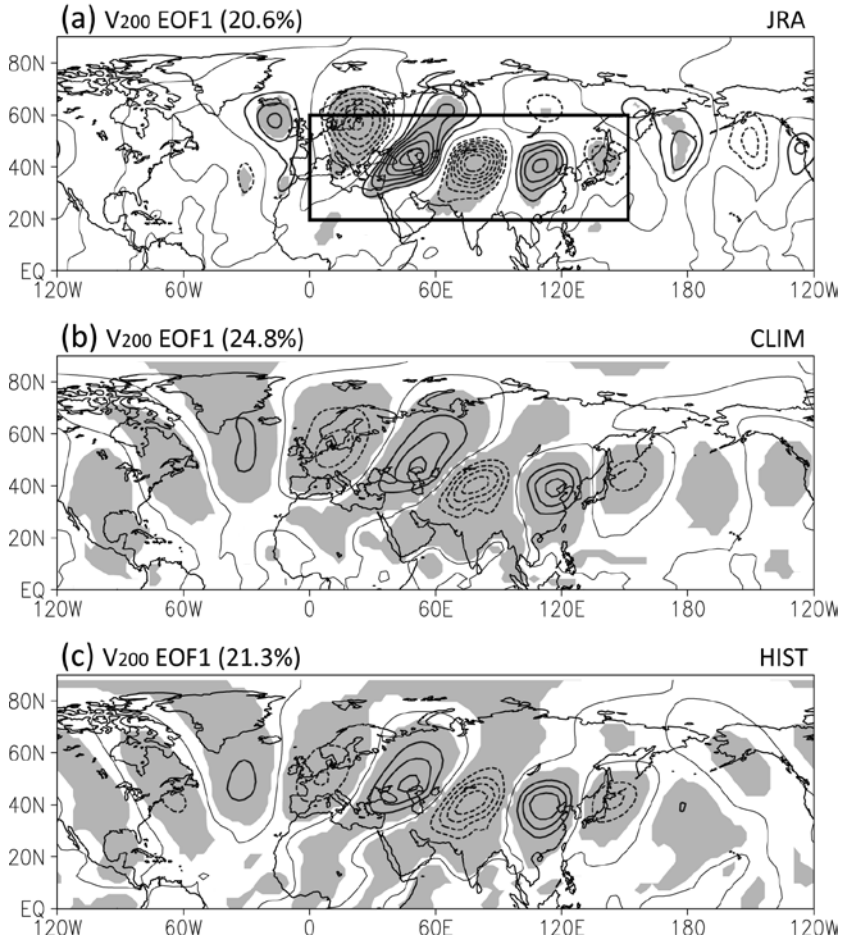

Fig.4 Leading EOFs to V200 in JJA during 1980-2004: (a) JRA25, (b) CLIM, and (c) HIST, as presented by the linear regression of V200 anomalies on to the associated PC time series. The EOF is performed over the Eurasian region of 0°-150° E, 20° -60° N (thick rectangle in (a)). The unit is m s^{-1} and the contour interval is 0.5 m s^{-1} exceeding $\pm$1 m s^{-1}. The shading indicates the anomaly significant at the 95% level.

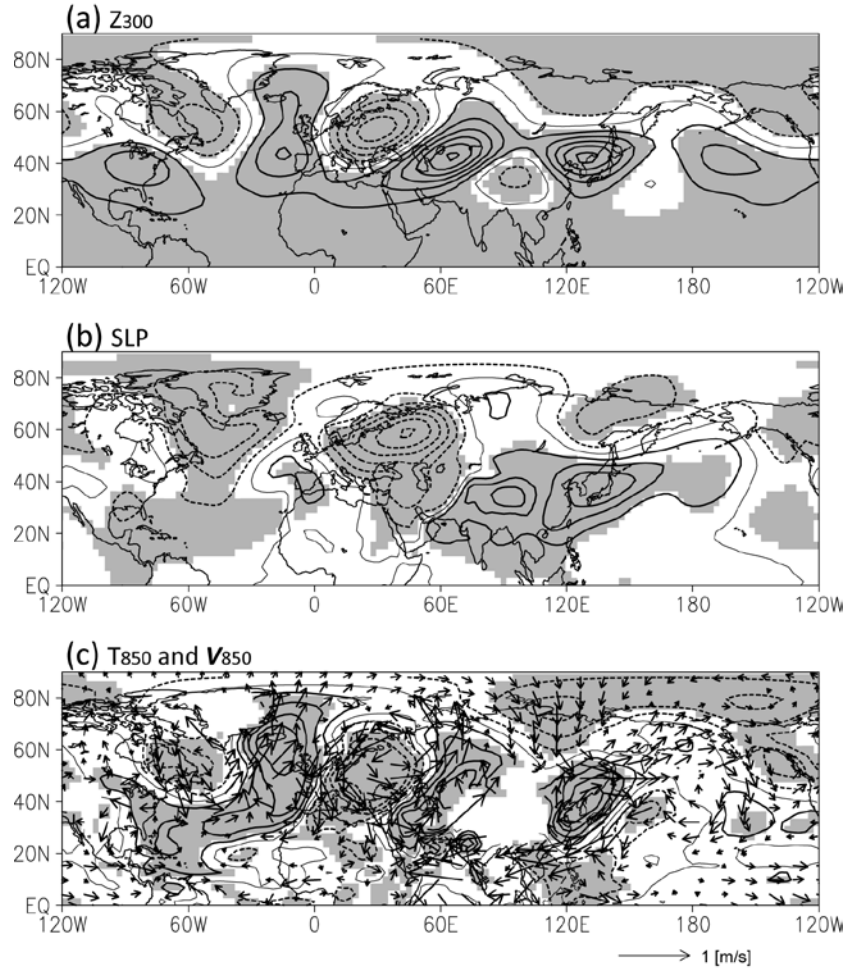

Fig.5 Monthly anomalies of (a) 300 hPa geopotential height (contour interval 5 m), (b) SLP (contour interval 0.2 hPa), and (c) temperature (contour; interval 0.1 K) and winds (vector) at 850 hPa, regressed upon the PC time series associated with the V200 EOF1 in HIST. The shading indicates anomalies significant at the 99% level.

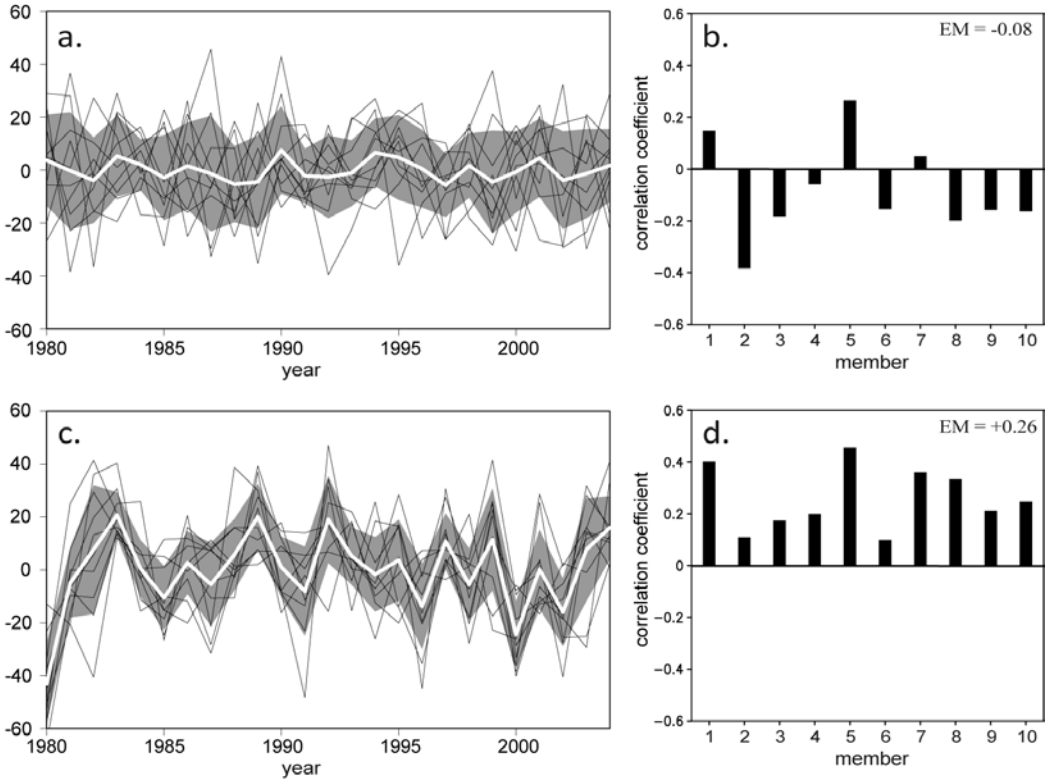

Fig.6 (a) PC time series of the EOF1 to V200 in CLIM. The PCs for each member are shown by thin curves, and the ensemble mean and its 1 SD are indicated by the thick white curve and shading. (b) Correlation coefficients of the PC time series for each member in (a) with that in JRA. (c)-(d) As in (a)-(b) but for HIST.

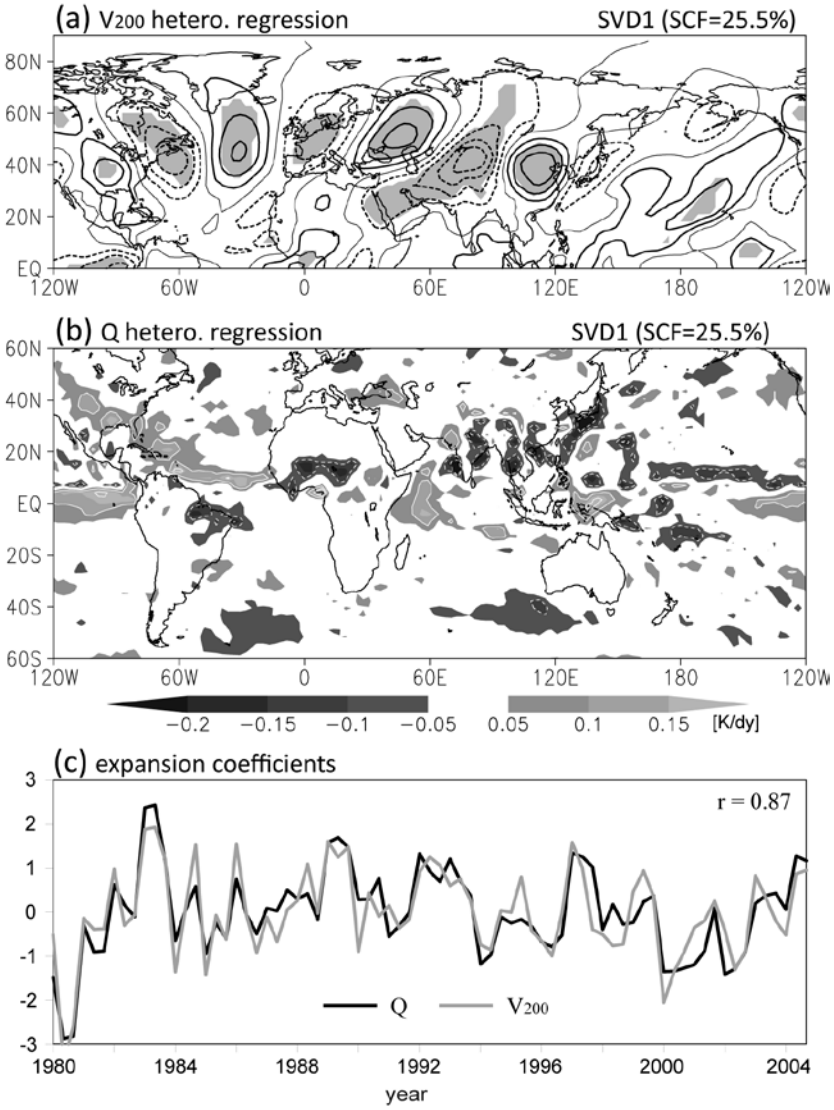

Fig.7 Leading SVD to monthly anomalies of V200 and $\widehat{Q}$ in JJA during 1980-2004: heterogeneous regression for (a) V200 and (b) $\widehat{Q}$, and (c) the expansion coefficients. The domain is the same as the EOF for V200 but is global for $\widehat{Q}$. Note that the V200 anomalies are the ensemble average. The contour interval is 0.3 m s^{-1} in (a) and 0.1 K day^{-1} in (b), and the shading indicates the anomaly significant at the 95% level.

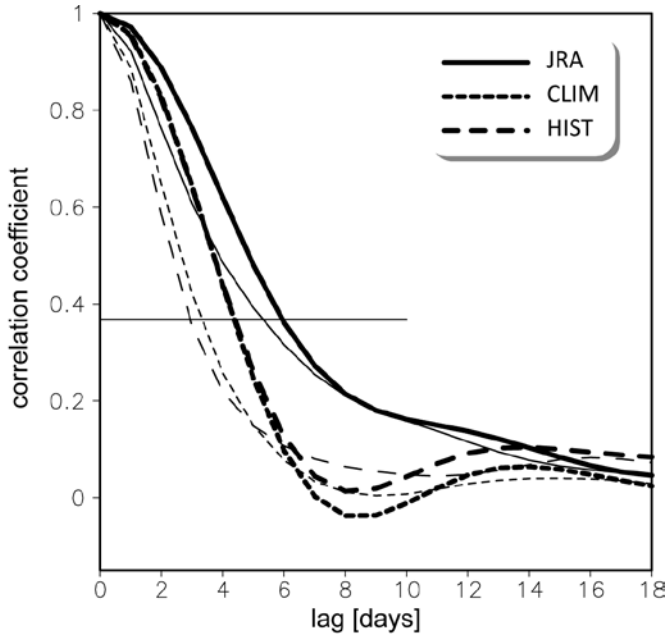

Fig.8 Autocorrelation functions for the low-frequency CGT index in JRA (solid), CLIM (dotted), and HIST (dashed). Autocorrelations for the unfiltered daily indices are also shown by thin curves. The crossing point between them and the horizontal thin line indicates the de-correlation time.

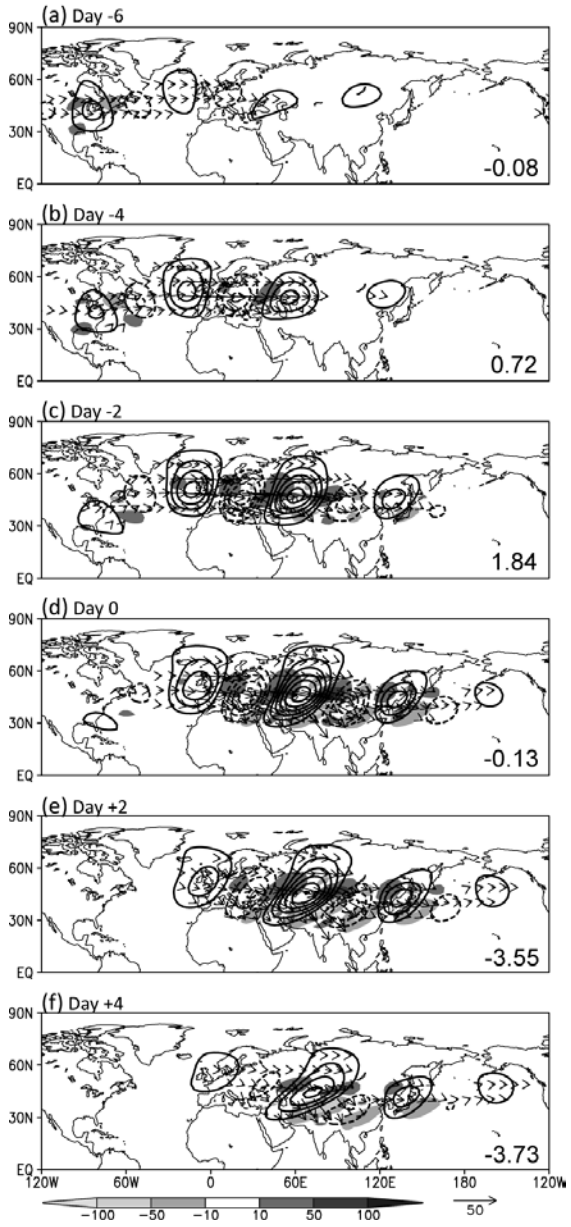

Fig.9 Time evolution of the composite low-frequency anomalies of the 200 hPa geopotential height (contour; interval 20 m) and the wave activity fluxes (vector) associated with the CGT pattern in HIST from (a) lag -6 days to (f) lag +4 days. Shown by shading is the barotropic energy conversion concurrent with the respective anomaly field. The energy conversion term averaged over 0°-150° E, 20° -60° N is also indicated at the bottom right of each panel.

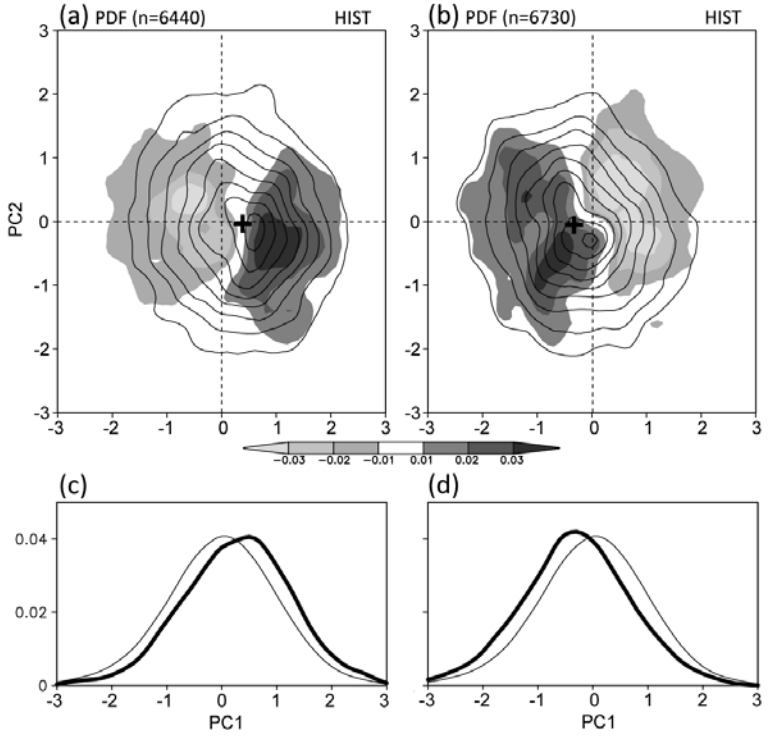

Fig.10 2D PDF for the low-frequency V200 anomalies (contour; interval 0.02) in JJA over the Eurasian region of 0° –150° E, 20° –60° N in the HIST, using samples when the SVD expansion coefficients for $\widehat{Q}$ (Fig. 7c) are (a) above 0.5 SD and (b) below –0.5 SD. The shading represents the deviation of the PDF from that calculated with all the available samples. The time-mean anomaly states are indicated by crosses. (c)-(d) As in (a)-(b) but for the 1D PDF along the PC1 axis (thick curve) superimposed on the PDF using all the samples (thin curve).

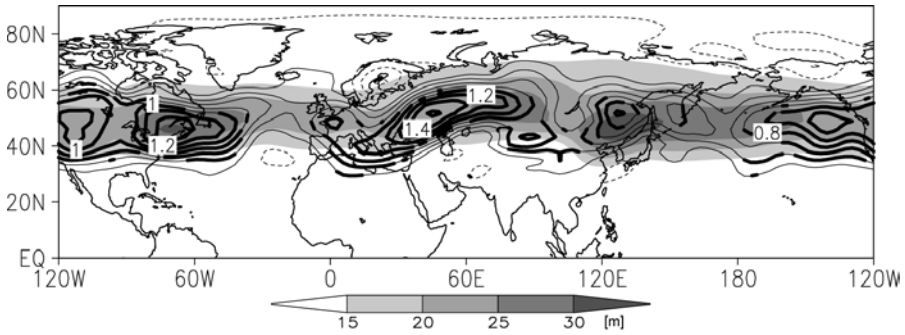

Fig.11 Anomalies of the storm track, $\sqrt{\overline{Z'^2}}$, at 500 hPa in the HIST (contour) regressed on the expansion coefficients associated with the SVD1. The contour interval is 0.2 m, and the anomalies significant at the 95 % level are shown by thick contours. The shading indicates the JJA climatology of $\sqrt{\overline{Z'^2}}$ at 500 hPa.

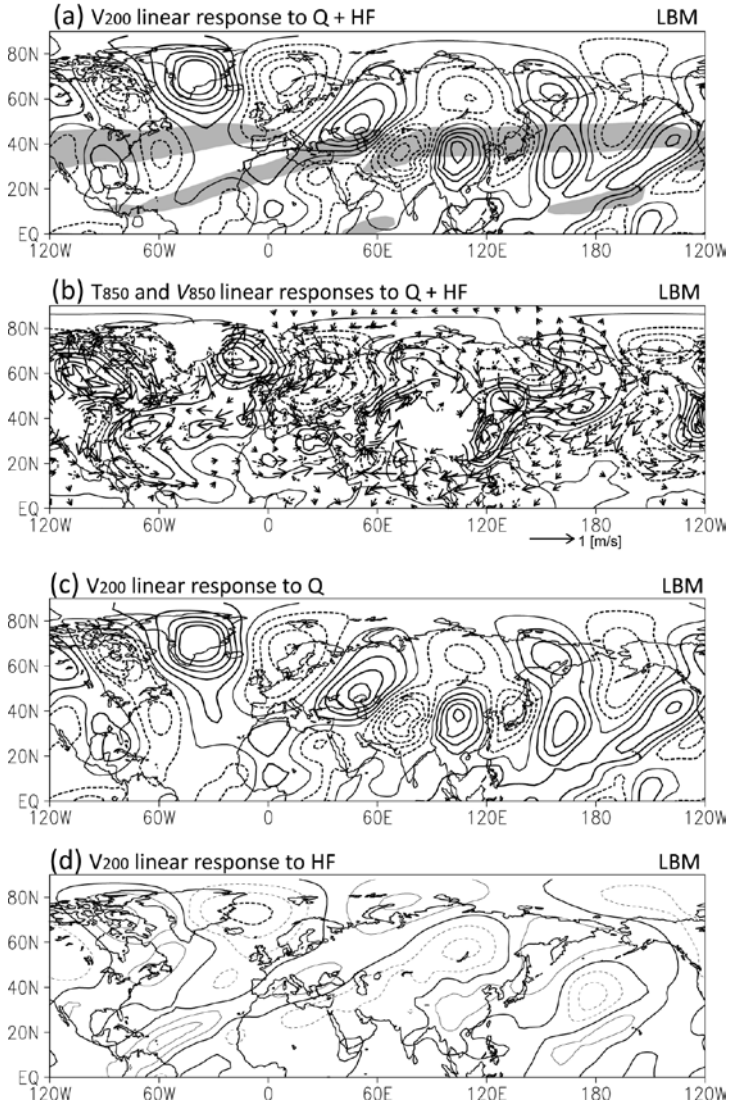

Fig.12 Steady linear response in (a) V200 (contour interval 0.3 m s^{-1}) and (b) temperature (contour; interval 0.1 K) and winds (vector) at 850 hPa to the sum of the anomalous diabatic heating and the high-frequency eddy forcing both associated with the SVD shown in Fig. 7b. (c)-(d) As in (a) but for the responses to the heating and the eddy forcing, respectively. The basic state is derived from the JJA climatology in HIST, and the shading in (a) indicates the effective beta of the basic state exceeding 3×10^{-11} m^{-1} s^{-1}. Supplemental contours (interval 0.1 m s^{-1}) are shown by thin lines in (d).

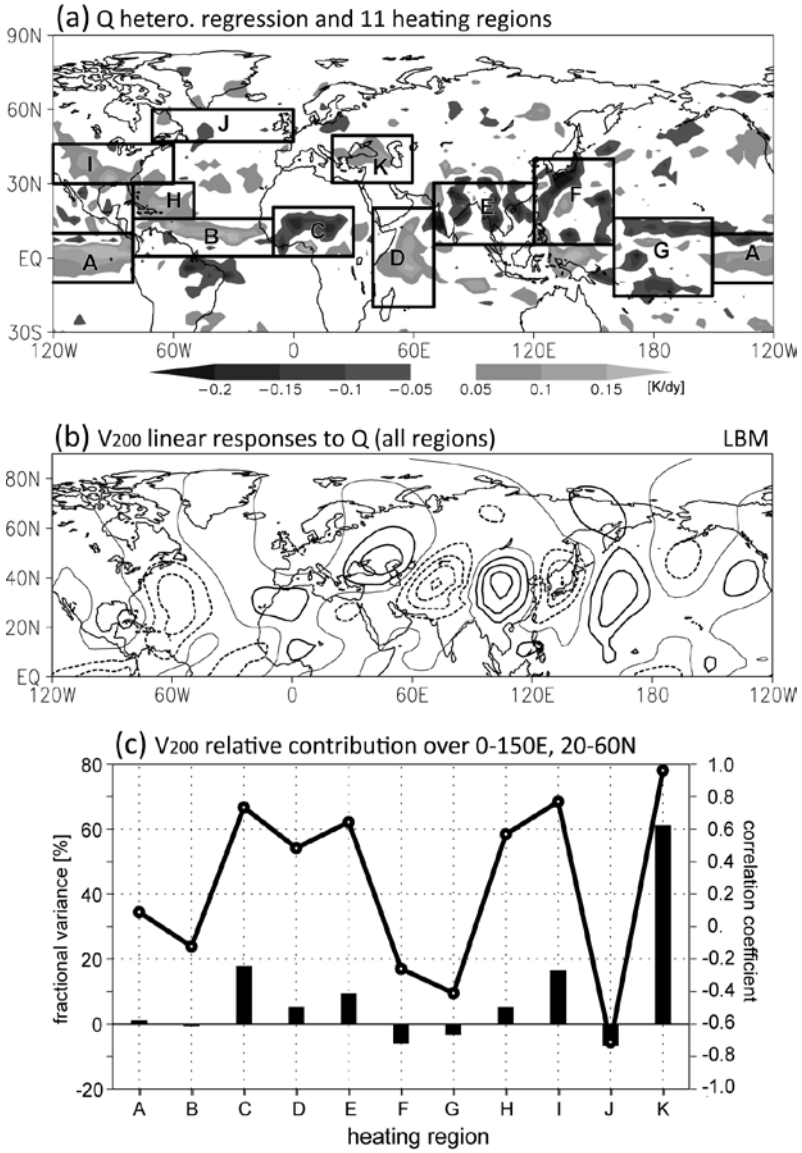

Fig.13 (a) Regional division of the diabatic forcing given to the LBM (boxes labeled from A to K) superimposed on $\widehat{Q}$ (shading, same as Fig. 7b). (b) As in Fig. 12c but for the response to the sum of the forcing over the 11 regions defined in (a). (c) Fractional variance (bars) and spatial correlation (curve) of the V200 response to each regional forcing with that shown in (b), evaluated over Eurasia of 0°-150° E, 20° -60° N.

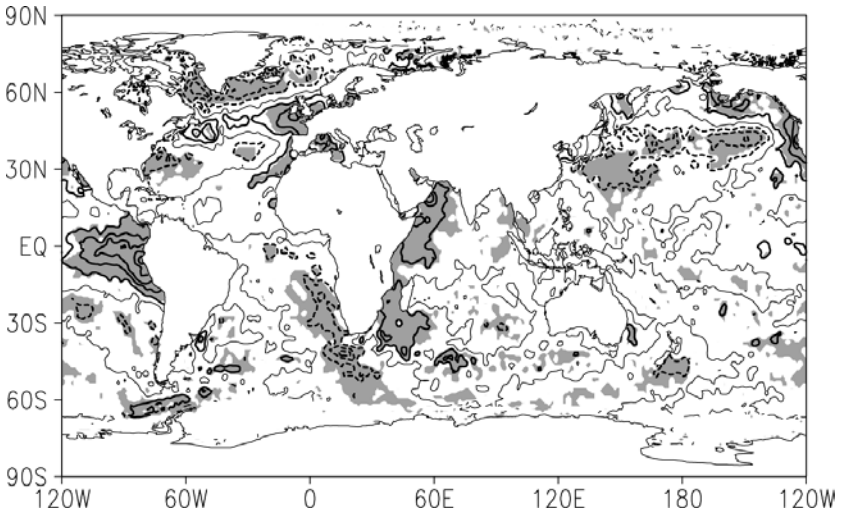

Fig.14 Monthly anomalies of SST in JJA regressed upon the SVD expansion coefficients for $\widehat{Q}$. The contour interval is 0.1 K and the shading indicates the anomalies significant at the 95% level.

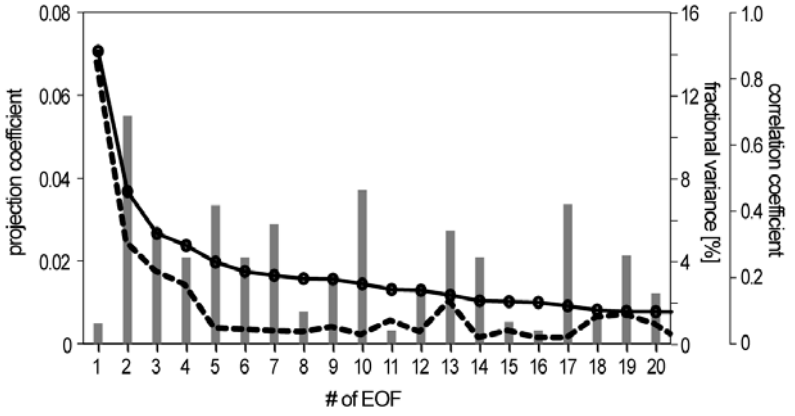

Fig.15 Fractional variance of the EOF (curve with circles) to monthly $\widehat{Q}$ in JJA over the tropics of 30°S -30° N, correlation between the PC time series and the Niño 3 SST anomaly (dashed curve), and the spatial projection coefficients of the SVD1 for $\widehat{Q}$ (Fig. 7b) on to the EOF patterns (bars). The projection only measures the similarity of the horizontal structure, so that the sign of eigenvectors are reversed if the projection is negative.

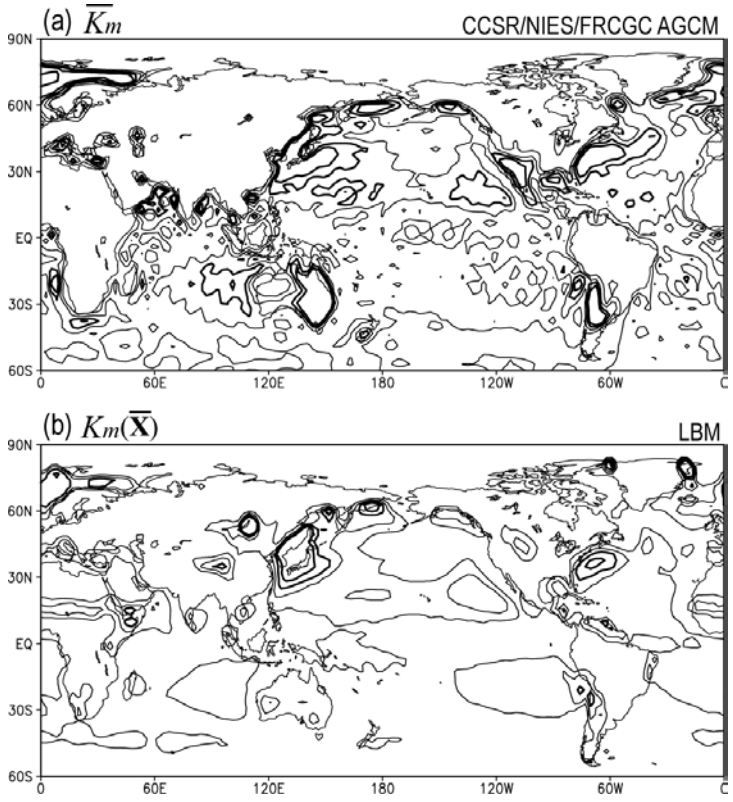

Fig. A1 The vertical diffusion coefficients for momentum at σ=0.98, obtained from (a) the climatology in the AGCM and (b) linearized turbulence closure in the LBM. The contour interval is 20 m^2 s^{-1}, and the values above 60 m^2 s^{-1} are indicated by the thick contour.